Supplement of Atmos. Chem. Phys., 22, 16111–16122, 2022
https://doi.org/10.5194/acp-22-16111-2022-supplement

Atmospheric Chemistry and Physics
Open Access
EGU

Supplement of

Record-breaking statistics detect islands of cooling in a sea of warming

Elisa T. Sena et al.

Correspondence to: Ilan Koren (ilan.koren@weizmann.ac.il)

Supplementary material

1. Record-breaking statistics applied to GCM simulations

a) Pre-industrial control run:

Several analyses were done to compare the number of records in the modelled pre-industrial (PI control) outputs from the MRI-ESM2-0 CMIP6 GCM (which accounts only for internal variability of the climate system – without an increase in GHG since 1850) with that of a TFRV. Histograms of ρ and of the high and low observed number of records over the TFRV expected values (R(n)/H(n)) show that for the model's PI control realizations, these metrics are much closer to that of TFRV than the results we got from the observational SST dataset (ERSST-v5). While for the observations (Fig. 2 of the main paper), the peaks of the distribution the number of high (low) records were positioned clearly above (below) the expected TFRV value, for the PI control run samples, the peak of the *R(n)/H(n)* distributions is at 1 (Figure S1 below). The comparison between the histograms of ρ confirm this result. For the observations, the distribution peaks much higher than 0 (Fig. 2 of the original manuscript), while in the Figure S1 below, ρ peaks at 0. The distributions shown in Figure S1 are almost identical to the distributions of the same metrics obtained from a TFRV. In fact, even though the internal variability alone is expected to increase the number of record highs and record lows evenly, the variance of the TFRV and the GCM PI control runs histograms are remarkably similar. The expected standard deviation of the records of a TFRV is 1.8, and the model's PI control realizations have a standard deviation of 1.9. Overlapping histograms of ρ and its cumulative frequency for the modelled PI control run samples and for Monte-Carlo simulations for a TFRV show how similar these distributions are (Figure S2). This similarity of the records distribution drawn from the GCM PI control with the TFRV distribution gives us more confidence in the capability of record-breaking statistics to verify trends climate time series and, once again, confirms the robustness of this method.

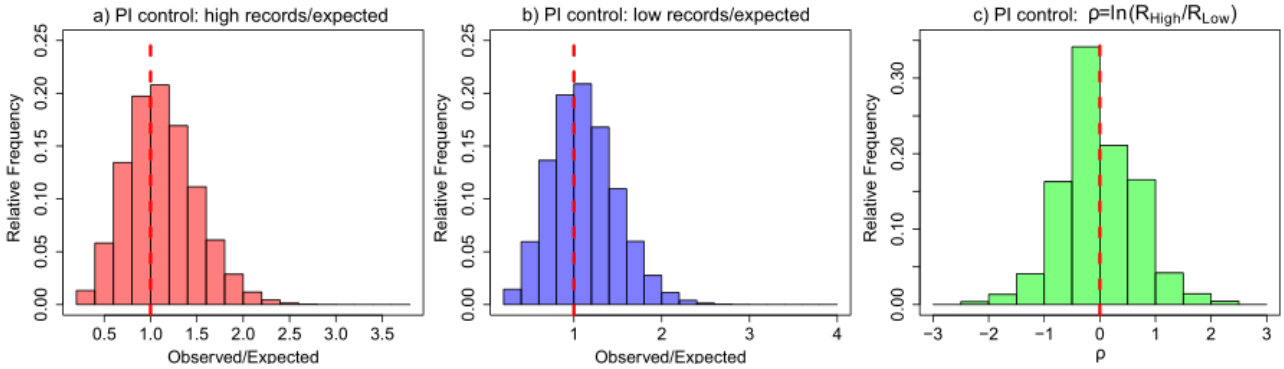

Figure S1: Histograms of observed over expected number of records and ρ for the PI control run samples of the MRI-ESM2-0 CMIP6 global climate model.

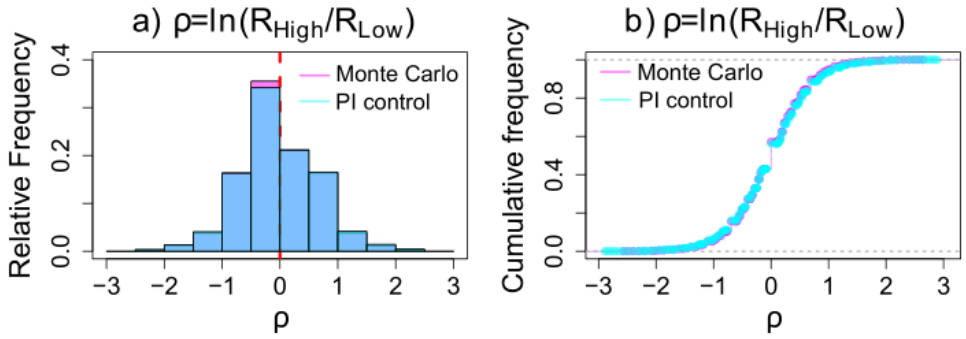

Figure S2: Comparison between the frequency distribution of ρ for the MRI-ESM2-0 PI-control run samples and Monte Carlo simulations of a TRFV.

Figure S3 shows the mean spatial distribution of the high and low *R(n)/H(n)* and ρ calculated from 1000 maps of the number of records (each of them for a random 75-year sample) of the modelled PI control run samples. We observe that the spatial pattern is almost homogeneous with weak values of *R(n)/H(n)* and ρ (close to 1 and 0, respectively). Unlike the observational results, there are no robust cooling or warming islands in these maps. The cooling and warming regions are due to sampling fluctuations, in contrast to our observational results

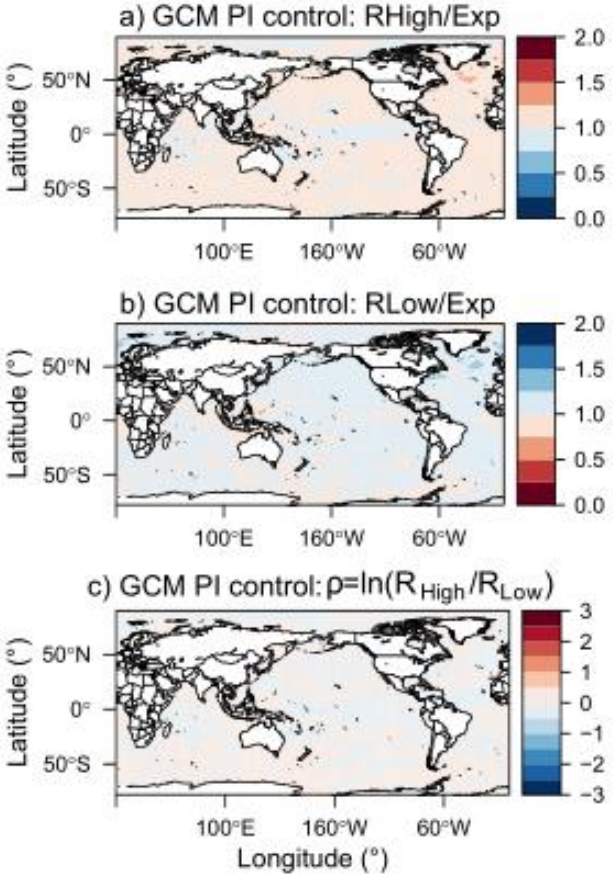

Figure S3: Mean spatial distribution of the high and low *R(n)/H(n)* and ρ calculated from 1000 maps of the number of records (each of them for a random 75-year sample) of the modelled MRI-ESM2-0 PI control run samples.

The CDFs of the high and low records compared to the theoretical CDF of number of records of a TFRV again point to the similarity of these distributions (Figure S4). The Kolmogorov-Smirnov (KS) test shows the following statistics for the MRI-ESM2-0 PI-control run samples:

D_{HIGH} = 0.041
D_{LOW}= 0.035

The statistics of the test indicate that the number of records of the MRI-ESM2-0 PI control run samples are significantly different from those expected for a TFRV distribution, both for R_{High} and R_{Low}. However, for the observations reported in the main text, we obtained much higher *D* values, around 0.3 (far off the scale of the figure).

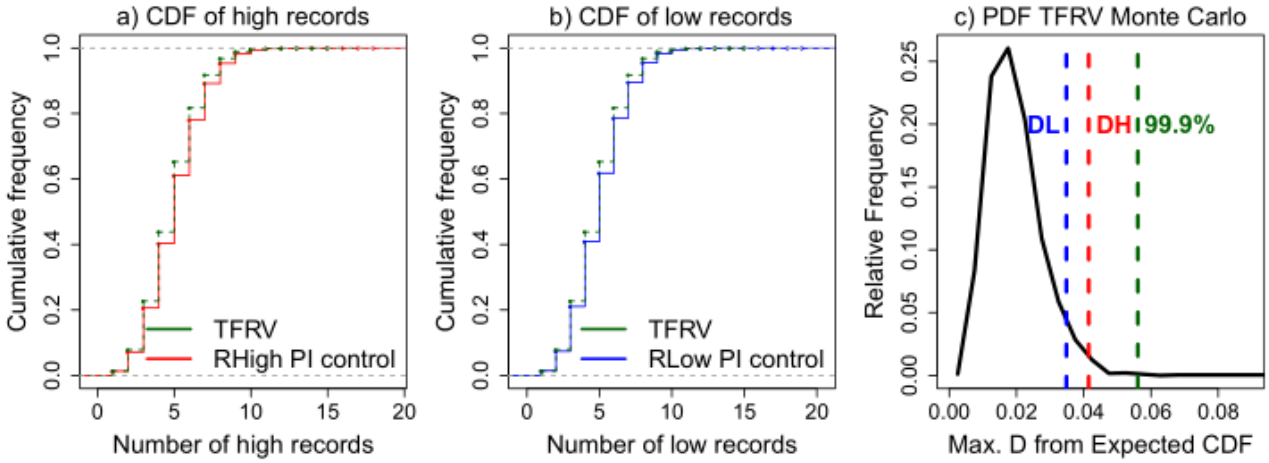

Figure S4: Cumulative frequency distributions of the high and low number of records for the MRI-ESM2-0 PI-control run samples compared to the TRFV distribution (a and b). Panel c shows the results of the statistics *D* of the Kolmogorov-Smirnov (KS) test for PI-control run samples compared to the distribution of *D* we would get from TFRV Monte Carlo simulations.

The distribution of the deviation from expectancy (in standard deviation units) of the PI control run samples also peaks at 0 (Figure S5), unlike our results for the observational dataset, which were clearly shifted to positive values in the case of high records and negative values for low records (Figure 5 of the main text).

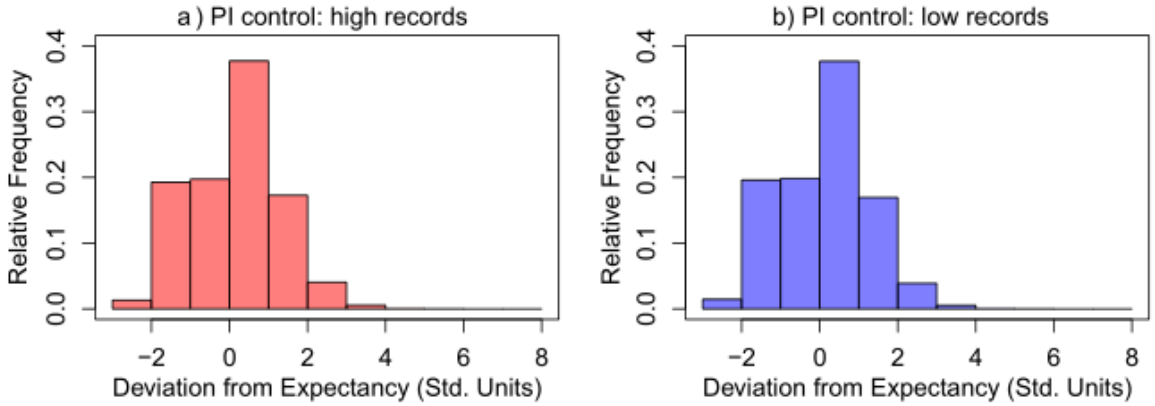

Figure S5: Histograms of the high and low deviation from expectancy of the number of records for PI control run samples of the MRI-ESM2-0 CMIP6 global climate model.

b) Study period (1946-2020):

Record breaking statistics was also applied to the MRI-ESM2-0 simulations during the same time period as used in our observational analysis (1946-2020). For that, a combination of the historical data set and scenario projection 2 (SSP2-4.5) was used. The spatial distribution and histograms that resulted from these analyses are shown in Figure S6. They show that the excess of records highs over the TFRV expected value is similar to observations, while the distribution of the low *R(n)/H(n)* peaks around 1, resulting in positive but smaller values of ρ relative to the observational results, shown in Figure 2. The boxplots shown in Figure 6 of main text also help to interpret these results. Note the resemblance of the spatial patterns of this global model simulation (Figure S6) and the observation-based results (Figure 2 of the main text). There are some cooling regions in North Pacific and North Atlantic and a cooling spot in the Southern Ocean, just like the features in the results from the observational data set (Figure 2). There is also cooling in the Indian Ocean, between Africa and Australia and the east coast of South America. These two features also appear in Figure 2.

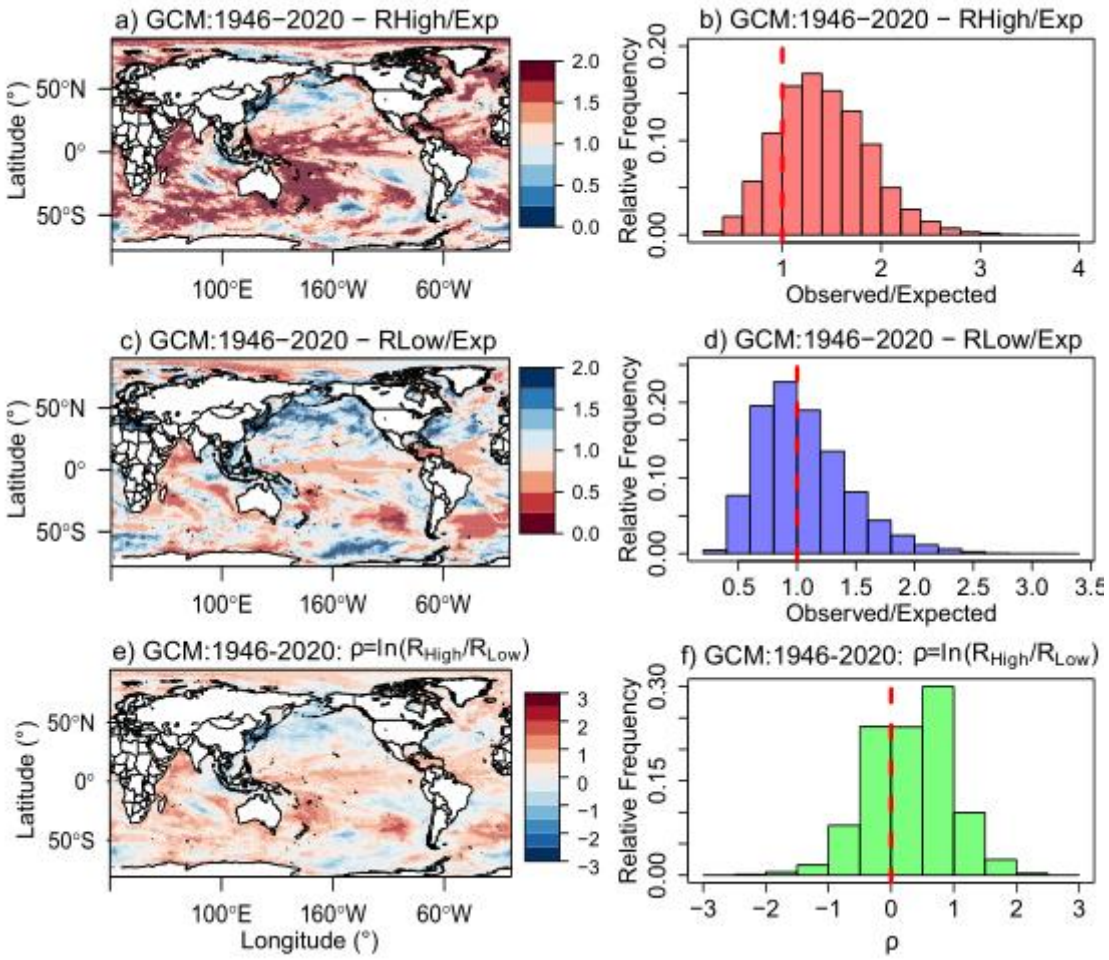

Figure S6: Spatial distribution and histograms of observed over expected number of records and ρ for the SST of the MRI-ESM2-0 CMIP6 global climate model during the study period (1946-2020).

c) Scenario projection SSP-2 4.5:

To test the forecast distribution of the number of records projected by GCMs, record breaking statistics on the scenario projection SSP-2 4.5 of MRI-ESM2-0 CMIP6 model, between 2015 to 2100 were applied. This model predicts that in the future the high record breaking will be even more frequent than in the present, while low record breaking will be less frequent (Figures S7 and 6). At least two cold spots are noticeable: a large one south of Greenland (presently known as the cold blob, already discussed in the original manuscript), and a second one in the Southern Ocean, southeast of Australia, which could be related to the cold spot we discovered in the historical observational data set ERSST-v5.

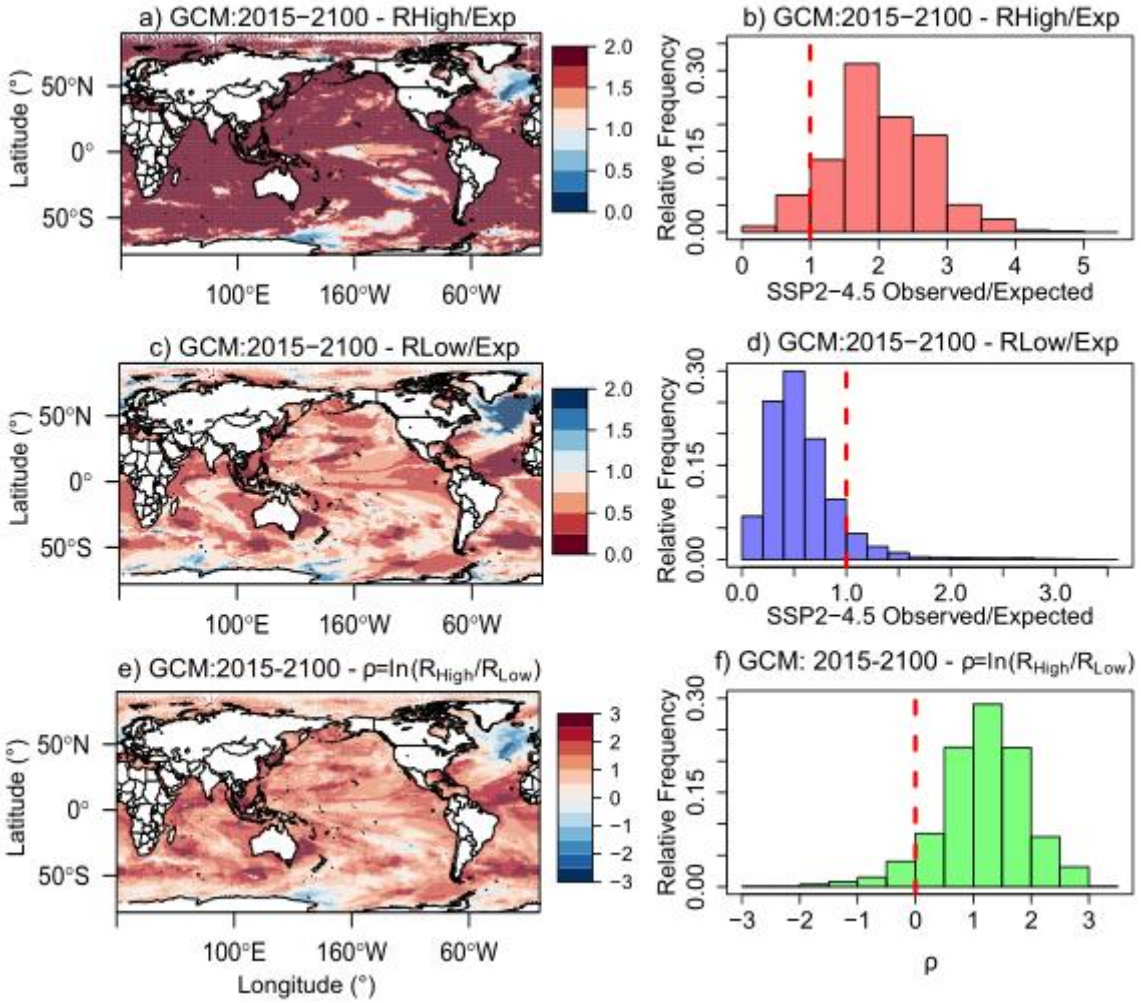

Figure S7: Maps and histograms of observed over expected number of records and ρ for the SST projections (SSP2-4.5) of the MRI-ESM2-0 CMIP6 global climate model from 2015-2100.

2. Record-breaking statistics applied to another observational dataset (HadISST)

To test consistency of our results, record-breaking statistics was applied to an alternative observational dataset, HadISST (https://climatedataguide.ucar.edu/climate-data/sst-data-hadisst-v11). Overall, the results point to similar conclusions for either of the two data sets. As ERSST-v5 (the original dataset used in this study), HadISST also presents an asymmetry in the number of records, with more high than low records (Figure S8). However, for HadISST the number of high records that surpass the TFRV expected value is 96% (as opposed to 83% for the ERSST-v5 data set). Furthermore, HadISST shows weaker ρ values than ERSST-v5 results. There are some features worth mentioning in the spatial pattern as well, such as the cooling spots in the North Pacific and North Atlantic, that also showed up in Figure 2 of the main text. The cold spot in the Southern Ocean is not evident in this data set, though. It is worth mentioning, however, that a new version of this dataset, HadISST-v2 is about to be released (https://www.metoffice.gov.uk/hadobs/hadisst2/data/download.html). To date only sea ice concentration was available from this newest version. Notice, however, that ERSST-v5 already uses Hadley Centre version 2 ice-SST concentration (HadISST-v2) as an input. Thus, record-breaking statistics respond to the improvements in this newest version, for the Southern Ocean, in particular.

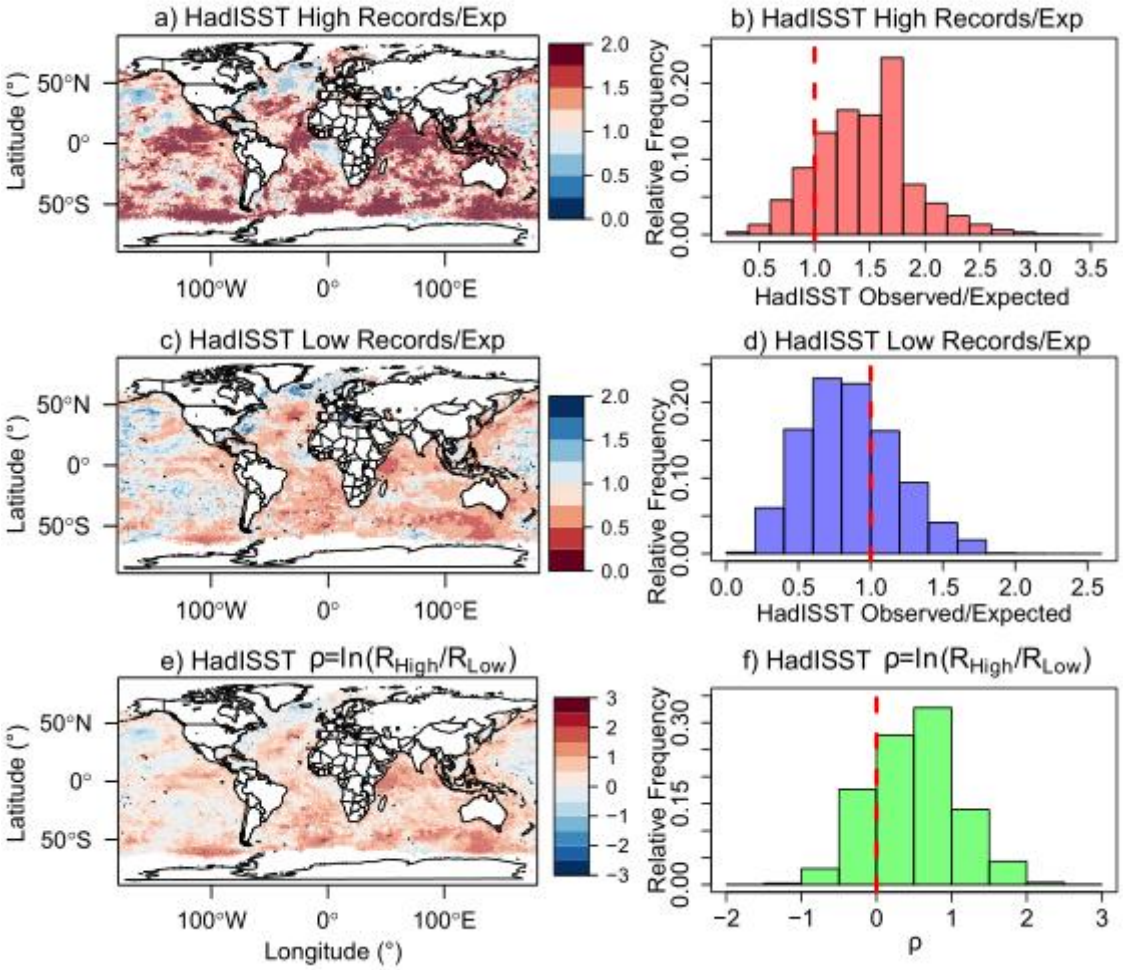

Figure S8: Spatial distribution and histograms of observed over expected number of records and ρ for the observational HadISST data set during the study period.

3. Removing the contribution of natural factors

To quantify how the internal variability of the system influences the number of records, a correction was applied to the dataset to remove the contribution of natural factors (ENSO, volcanic and solar signals) from SST. For that, a multiple linear regression of globally-averaged SST anomaly against a linear term and lagged time series of standardized southern oscillation index (SOI) (https://psl.noaa.gov/gcos_wgsp/Timeseries/SOI/), volcanic aerosol optical depth (τ) from Sato et al., 1993 (https://data.giss.nasa.gov/modelforce/strataer/) and total solar irradiation (TSI) index (https://www.ncei.noaa.gov/data/total-solar-irradiance/access/monthly/) was performed for the study period (Foster and Rahmstorf 2011, Lean and Rind, 2009). Table S1 shows the time lags (in months) used and the resulting coefficients for each term.

Table S1: Lags and coefficients from the multiple linear regression of SST anomaly by the several indexes.

	Lag (months)	Coefficients
Linear term	-	0.0089 ± 0.0001
TSI	0	0.006 ± 0.002
SOI	3	-0.035 ± 0.002
τ	11	-0.030 ± 0.002

For each pixel, the contribution of each natural forcing was removed from the SST. Figures S9 and S10 show, respectively, the time series of the mean global SST anomaly, and maps of high and low records before and after removing the contribution of natural factors. It is evident from these figures that, aside from a small change in the color scale, the number of records remained practically invariant to this adjustment. This shows that the record breaking

statistics is indeed robust and can be used to find trends in climate time series, despite the internal variability of the system.

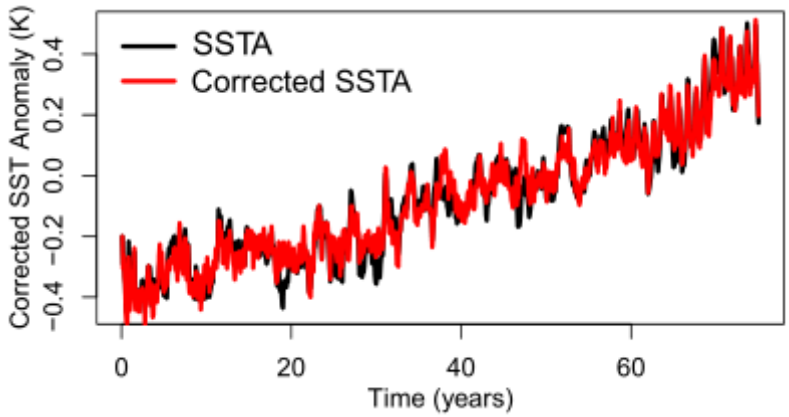

Figure S9: Time series of the mean global SST anomaly before and after the removal of the contribution of natural internal variability.

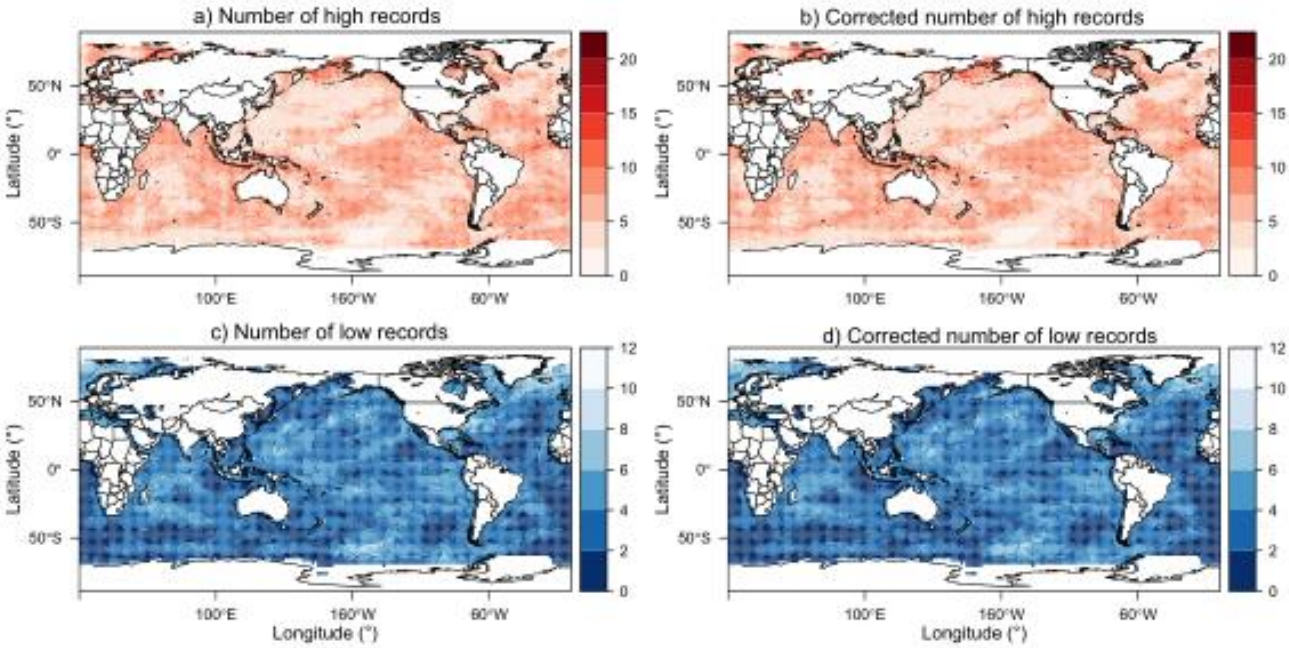

Figure S10: Spatial distribution of the number of high and low records before and after the removal of the contribution of natural internal variability.

References

Foster, G. and Rahmstorf, S.: Global temperature evolution 1979–2010, Environmental research letters, 6(4), 044022, https://doi.org/10.1088/1748-9326/6/4/044022, 2011.

Lean, J. L. and Rind, D. H.: How will Earth's surface temperature change in future decades?, Geophysical research letters, 36(15), https://doi.org/10.1029/2009GL038932, 2009.

Sato, M., Hansen, J. E., McCormick, M. P. and Pollack, J. B.: Stratospheric aerosol optical depths, 1850–1990, Journal of Geophysical Research: Atmospheres, 98(D12), 22987-22994, https://doi.org/10.1029/93JD02553, 1993.